Available online at www.sciencedirect.com

jmr&t
Journal of Materials Research and Technology

journal homepage: www.elsevier.com/locate/jmrt

Original Article

Piezo-photocatalytic activity of $Bi_2VO_{5.5}$ for methylene blue dye degradation

Manish Kumar [a], *Rahul Vaish* [a], *Zainab Mufarreh Elqahtani* [b], *Imen Kebaili* [c,d], *M.S. Al-Buriahi* [e], *Tae Hyun Sung* [f], *Wonseop Hwang* [f], *Anuruddh Kumar* [g,*]

[a] *School of Mechanical and Materials Engineering, Indian Institute of Technology Mandi, Mandi, Himachal Pradesh 175005, India*
[b] *Department of Physics, College of Science, Princess Nourah bint Abdulrahman University, P.O. Box 84428, Riyadh 11671, Saudi Arabia*
[c] *Department of Physics, Faculty of Science, King Khalid University, P.O. Box 9004, Abha, Saudi Arabia*
[d] *Laboratoire de Physique Appliquée, Groupe de Physique des matériaux luminescents, Faculté des Sciences de Sfax, Département de Physique, BP 1171, Université de Sfax, 3018 Sfax, Tunisia*
[e] *Department of Physics, Sakarya University, Sakarya, Turkey*
[f] *Department of Electrical Engineering, Hanyang University, 222, Wangsimni-ro, Seongdong-gu, Seoul 04763, South Korea*
[g] *Center for Creative Convergence Education Hanyang University, 222, Wangsimni-ro, Seongdong-gu, Seoul 04763, South Korea*

ARTICLE INFO

Article history:
Received 31 July 2022
Accepted 30 September 2022
Available online 15 October 2022

Keywords:
$Bi_2VO_{5.5}$
Photocatalysis
Piezocatalysis
Piezo-photocatalysis
Germination index

ABSTRACT

This study comprises the combined effect of piezocatalytic and photocatalytic activity to obtain improved piezo-photocatalytic dye degradation efficiency in visible light. Single-phase $Bi_2VO_{5.5}$ powder was prepared through solid-state synthesis at 750 °C in 8 h. Time-dependent photocurrent responses were conducted to understand the phenomenon of charge carrier transport in visible light. $Bi_2VO_{5.5}$ powder sample demonstrated high photocatalytic efficiency and good reusability possessing a bandgap value of 2.13 eV. $Bi_2VO_{5.5}$ powder sample attained ~70% and ~ 58% degradation efficiency during photocatalysis and piezocatalysis respectively. The piezo-photocatalytic methylene blue dye attained ~82% degradation efficiency in 240 min duration of visible light illumination. The scavenger test depicted holes (h^+) as the principal active species in the piezo-photocatalytic dye degradation. There incurred no severe loss in photocatalytic efficiency even after 4 cycles which proclaims the reusability of the $Bi_2VO_{5.5}$ powder sample. A study on the kinetic rate constant with varying dye concentrations was conducted. With varied dye concentration of 5, 10, 15 mg/L, the kinetic rate constant obtained was 0.00528, 0.0030, and 0.00125 min^{-1}, respectively. Germination index was found through a phytotoxicity test using vigna radiata seeds. Here visible light along with mechanical energy has been used to achieve higher MB dye degradation efficiency through piezo-photocatalysis.

* Corresponding author.
E-mail address: anuruddh07@hanyang.ac.kr (A. Kumar).
https://doi.org/10.1016/j.jmrt.2022.09.130

1. Introduction

At present time, a surge in water pollution has been a major concern across the globe. Various pollutants such as heavy metals, organic dyes, drugs, heavy metals, etc. are readily discharged into water bodies through domestic sewage and industrial wastewater. Textile industries are the major source of discharge of dye effluents causing water pollution [1,2]. Lack of proper treatment and handling aids in the surge of water pollution [3]. Organic dyes need special treatment for their eradication which is essential for environmental safety as they are not self-degradable [4,5]. Conventional wastewater treatment measures like ultra-filtration, microbial degradation, adsorption, and coagulation are general water treatment measures but these possess difficulty in low concentration of contaminants removal as well as lower removal efficiency [6,7]. Recently, photocatalysis has been used for dye degradation since it possesses advantageous features such as oxidation of contaminants at a low concentration at room temperature, non-toxicity, diminished secondary pollution, and low-cost [8,9]. At present time, anatase TiO_2 has been readily used as a commercial photocatalyst owing to its features such as good chemical stability, low cost, and high oxidizing power. However, TiO_2 functions in ultraviolet (UV) illumination because of its wide band gap (3.20 eV) and it has a short lifespan of photo-induced charge carriers leading to lower dye degradation efficiency [3,10]. We know visible light are in majority of the solar light spectrum (~40%) while UV light constitutes very less (~5%). These two factors probe hindrance towards its commercial applicability and efficient solar energy utilization [11,12]. Thus, there has been a great emphasis to develop a more efficient visible light active photocatalyst over recent years. In this regard, a great emphasis has been laid on developing a Bi-based photocatalyst that would be visible light active due to its readily availability of raw materials at low cost and its distinct electronic structure [13]. $BiVO_4$, Bi_2WO_6, $CaBi_2O_4$, $BaTaO_4$, $BiNbO_4$, Bi_2MoO_6, etc. are some of the recently reported bismuth-based photocatalysts [14,15]. As hybridized Bi (6s) and O (2p) valence bands are present, the Bi^{3+} containing oxides demonstrate photocatalytic properties [14,15].

In this present work, we are intended in exploring $Bi_2VO_{5.5}$ (BV) which is a member of the Bi–V–O system. Due to the presence of cadmium, most yellow pigments possess toxicity but bismuth vanadate is known for its ionic conductivity and non-toxic nature. These are highly stable and show a high price-to-performance ratio in comparison to organic pigments [16]. $Bi_2VO_{5.5}$ is known to possess a wide visible light response and its layered structure helps in efficient carrier transportation [16]. BV possesses crystal structure and elemental composition similar to $BiVO_4$ [17]. Moreover, the visible light absorption range of BV is larger than $BiVO_4$ owing to its reduced bandgap (2.13 eV) [18,19]. $Bi_2VO_{5.5}$ or $Bi_4V_2O_{11}$ [20] belongs to the Aurivillius family possessing the general formula $(Bi_2O_2)^{2+}$ $(A_{n-1}B_nO_{3n+1})^{2-}$, where A refers to tri-, di- or mono-valent ions or their mixture, B refers to hexa-, penta- or tetra-valent ions and n refers to counts of the perovskite blocks sandwiched in between the (Bi_2O_2) layers [21]. $Bi_2VO_{5.5}$ possess ferroelectric property below 725 K [21–24]. $Bi_2VO_{5.5}$ is one of the eminent ferroelectric materials [25]. Ferroelectric materials show permanent spontaneous polarization (P_s) below Curie temperature (T_c). The non-centrosymmetric unit cell caused to erupt discrete stable polarization inducing spontaneous polarization in the material. Band bending and space charge regions arise as a result of the resultant surface polarization [26]. At low temperatures, oxygen vacancies linked to vanadium atoms form vanadium centered octahedral and tetrahedral. Elevated high temperatures disrupt the oxygen vacancies thereby causing high oxide-oxygen conductivity [27–29]. Wang et al. achieved 95% methyl orange degradation efficiency in visible light using $BiVO_4/Bi_2VO_{5.5}$ nanostructure [30]. Xie et al. achieved 85.2% degradation of methylene blue (MB) in the visible range using Au nanoparticles loaded on $Bi_2VO_{5.5}$ [31]. Liang et al. achieved 99% rhodamine B degradation in the visible range using $TiO_2/Bi_4V_2O_{11}$ photocatalyst [32]. Lu et al. has degraded MB dye in the visible range using $Bi_4V_2O_{11}$ photocatalyst [33]. Kumar et al. has shown RhB and MB dye degradation in UV irradiation using $Bi_4V_2O_{11}$ [16]. Xie et al. achieved 89.97% MB dye degradation in simulated sunlight using $Bi_2VO_{5.5}/Bi_2O_3$ composite films [19]. Piezocatalysis is known for pollutant degradation utilizing ultrasonic vibration as an excitation source [34]. The non-centrosymmetric orthorhombic structure of BV imparts piezoresponsive behavior [35,36].

Recently, we reported 81% piezo-photocatalytic degradation efficiency of MB dye using a $BiVO_4$ sample [37]. In the present work, we have tried to explore $Bi_2VO_{5.5}$ (BV) from the same Aurivillius family as that of $BiVO_4$. We have used visible light along with mechanical energy to achieve higher MB dye degradation efficiency through piezo-photocatalysis. The synergistic combined piezo-photocatalysis effect facilitates easy electron-hole pair separation and thus reduces the photocatalysis time at the same time attains high dye degradation performance. Bare piezocatalytic study and combined piezo-photocatalytic activity with $Bi_2VO_{5.5}$ has not been explored till now and this approach would open a new door to be utilized for water pollution eradication at the industrial level.

2. Experimental

2.1. *Fabrication of $Bi_2VO_{5.5}$ powder*

$Bi_2VO_{5.5}$ ceramic powder was prepared using Bi_2O_3 and V_2O_5 as the starting raw materials taken as per the ascribed stoichiometric molar ratio. These powders are initially mixed manually in a mortar pestle for nearly 30 min and the acquired homogenous mixture was calcined at 750 °C for 8 h duration to obtain the $Bi_2VO_{5.5}$ phase. The preparation methods of $Bi_2VO_{5.5}$ ceramic powder are displayed in Scheme 1.

2.2. *$BiVO_{5.5}$ powder characterization*

Phase identification of the BV powdered samples was assured by the X-ray diffraction (XRD, Rigaku diffractometer, Japan,

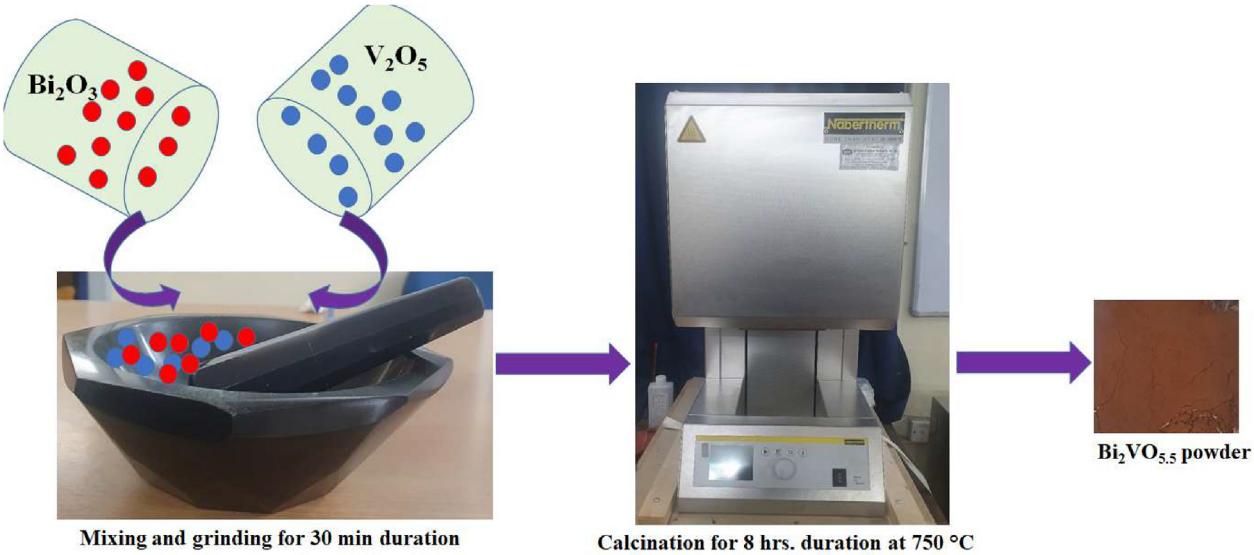

Scheme 1 – The preparation process for the BV powder.

9 kW, Cu–K α rotating anode) technique. The sample powder was put through a 2°/min scan rate over the 2θ angle ranging from 10 to 60°. To understand the existing bonding and structure in the sample Raman spectroscopy was done. HORIBA (LabRAM HR Evolution, Japan) spectrometer was used to acquire the Raman spectra where 532 nm laser excitation wavelength, 10% power, and 600 gratings were taken in use to scan the sample over the range of 350–1100 cm^{-1}. Perkin Elmer spectrum RX I spectrophotometer was used to conduct Fourier transform infrared spectroscopy (FTIR) analysis in the range of 500–1600 cm^{-1} where KBr pellets were used as sample matrix. To obtain the microstructures and the surface morphology of the samples Nova Nano SEM-450 scanning electron microscope (FE-SEM) was taken into use. Inbuilt energy dispersive spectroscopy (EDS) in SEM was taken into use to understand the compositional element distribution in BV powdered sample. Binding energy and the chemical state of the BV sample were obtained using the (Nexsa) X-ray photoelectron spectrophotometer instrument with an Al-Kα source. The absorbance peak intensity was obtained through the (SHIMADZU) UV–visible spectrophotometer instrument.

2.3. *Photocurrent measurement*

An electrochemical workstation (AUT86543 Metrohm Autolab B.V.) was utilized to obtain the current-time curves for the BV sample. Here three electrode setup was employed where the platinum wire served as a counter electrode, Ag–AgCl wire served as the reference electrode, and the working electrode while two bulbs of Havells Company (each 15W) served as the visible light illumination source. In order to get a photocurrent response, a few cycles of OFF and ON of the visible light source was conducted. 0.1 M phosphate-buffered saline solution served as electrolyte. To make the working electrode, 5 mg of catalyst was mixed in 1 mL of ethanol where an additional 20 μL Nafion solution was added, and utilizing this well-dispersed catalyst ink solution was prepared. The catalyst ink was subjected to 30 min of ultrasonication and thereby ~10 μL of catalyst ink was taken into use to coat the surface of the cleaned glassy carbon electrode. The coated electrode was properly dried before being used as the working electrode.

2.4. *Bandgap calculations*

To know the bandgap of the sample, diffuse reflectance spectroscopy (DRS) was used. The obtained absorption spectra from DRS were readily converted into Tauc's plot (a plot drawn between $(\alpha E)^2$ vs E) so as to get the direct bandgap as mentioned in many works of literature [38,39].

2.5. *Photocatalytic activity*

The photocatalytic assessment of the powdered BV was determined by degrading MB dye in visible light illumination. For conducting the catalysis experiment, 0.25 gm of powdered sample was used. Prior to the commencement of the photocatalysis assessment, adsorption saturation concerning the dye was attained precisely. On attaining adsorption saturation, the used dye is substituted with a new 10 ml dye volume of ~ 5 mg/L concentration as the initial starting dye. The powdered BV sample submerged in dye solution was placed in the visible light source coming from two bulbs (Havells company, each 15W power). The light source was confined at a distance of ~ 12 cm from the sample. An incessant stir at 500 rpm was provided all over the experiment. To obtain the adsorption peak intensity, a test sample was procured after a definite interval which was replenished again to the beaker to sustain a consistent volume. MB dye degradation percentage was evaluated as per Eq. (1) [40,41].

$$\%\ \text{removal of MB dye} = \frac{C_o - C}{C_o} \times 100 \quad (1)$$

where, C_o and C symbolize the MB dye concentration previously and after the passing of 't' time, respectively.

2.6. *Piezocatalytic activity*

The piezocatalytic performance of the powdered BV was determined by degrading MB dye in ultrasonic vibration. For conducting the catalysis experiment 0.25 gm of powdered sample was taken into use. Prior to the commencement of the piezotocatalysis assessment, adsorption saturation concerning the dye was attained precisely. On attaining adsorption saturation, the used dye is substituted with a new dye of volume 10 ml of ~ 5 mg/L concentration as the initial starting dye. BV powdered sample submerged in dye solution was subjected to ultrasonic vibration source coming from ultrasonicator (40 kHz, 150 W). Since the water was used as a medium during ultrasonication so, after elapse of every 15 min, the water was replaced from the ultrasonicator in order to shun dye solution heating. This experiment was conducted in dark conditions. To acquire adsorption peak intensity, a test sample was procured after a definite interval which was replenished again to the beaker to retain a consistent volume.

2.7. *Piezo-photocatalysis activity*

Piezo-photocatalytic assessment of the powdered BV was determined by degrading MB dye in the dual effect of visible light illumination and ultrasonic vibration. For conducting the catalysis experiment 0.25 gm of powdered sample was taken into use. Prior to the commencement of the piezo-photocatalysis assessment, adsorption saturation concerning the dye was attained precisely. On attaining adsorption saturation, the used dye is substituted with a new 10 ml dye volume of ~5 mg/L concentration as the initial starting dye. The BV powdered sample submerged in dye solution was subjected to a dual effect of visible light illumination coming from two bulbs (Havells company, 15W power each) and the ultrasonic vibration source coming from an ultrasonicator (40 kHz, 150 W). Since the water was used as a medium during ultrasonication so, after elapse of every 15 min, the water was replaced from the ultrasonicator in order to avoid dye solution heating. To get adsorption peak spectra, a test sample was procured after a definite interval which was replenished again to the beaker to retain a consistent volume.

3. Results and discussion

Fig. 1 displays the XRD pattern of the prepared BV powdered sample. The obtained XRD pattern conveys that all the diffracted peaks well match the perovskite layered structure of bismuth vanadate. The BV sample shows (orthorhombic) single phase which is in conformity to the standard JCPDS references file of orthorhombic $Bi_2VO_{5.5}$ (File No. 42–0135). There was no presence of any secondary peak which justifies $Bi_2VO_{5.5}$ single phase formation.

Sharp diffraction peaks depict higher crystallinity of the powdered sample. The % crystallinity of the powdered sample was evaluated using Eq. (2) [42–44].

$$\%\ \text{Crystallinity} = \frac{\text{Area under the crystalline peaks}}{\text{Area of all peaks}} \times 100 \qquad (2)$$

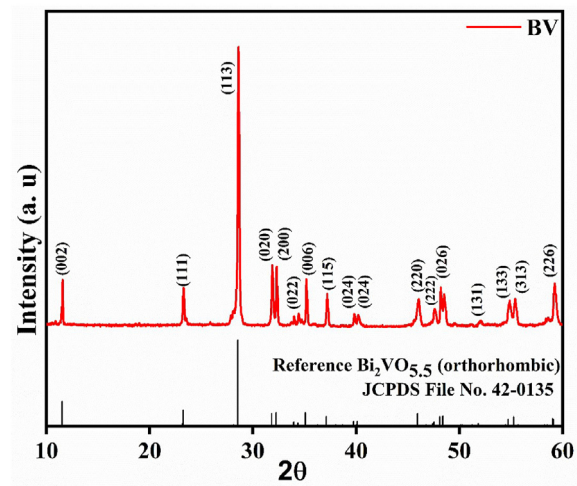

Fig. 1 – XRD of synthesized BV powder.

The evaluated % crystallinity of the sample was found to be 73%.

Fig. 2 shows the Raman bands associated with the prepared BV sample. Here, the Raman spectrum of BV was studied over the range of 350–1100 cm^{-1}. The Raman bands were discovered at 372, 653, 768, 852, and 925 cm^{-1}. These bands are consistence with that reported in the literature [16,45]. The band at 372 cm^{-1} is because of the vibrational mode symmetric bending of V–O bonds present in BV [16]. The band at 653 and 768 cm^{-1} are because of the doubly coordinated (V–O–V) oxygen atom. The presence of the Raman band at 852 cm^{-1} is because of the vibration of the short-range V–O bonds [45]. There is a presence of weak vibrational mode at 925 cm^{-1} because of the small amount of $V^{4+} = O$ unit. When vanadium is present in a mixed-valence state of a+5 and + 4, this vibrational mode is known to be the signature of $V^{4+} = O$ [45].

Fig. 3 shows the FTIR spectroscopy study to understand the change in the functional groups of the material. There is the presence of strong IR bands at 832, 766, 715, 610, and 529 cm^{-1}.

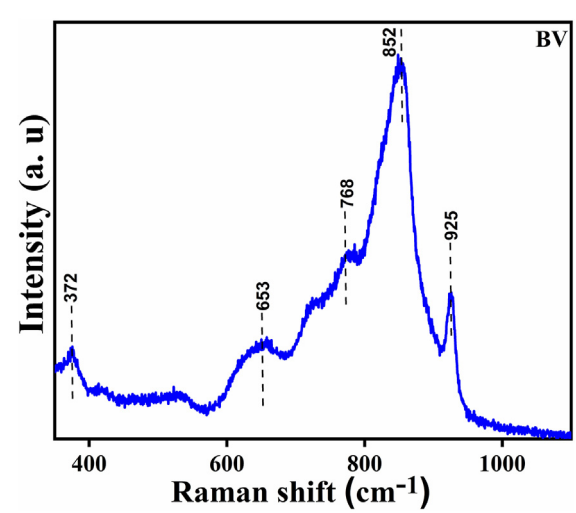

Fig. 2 – Raman spectrum of BV.

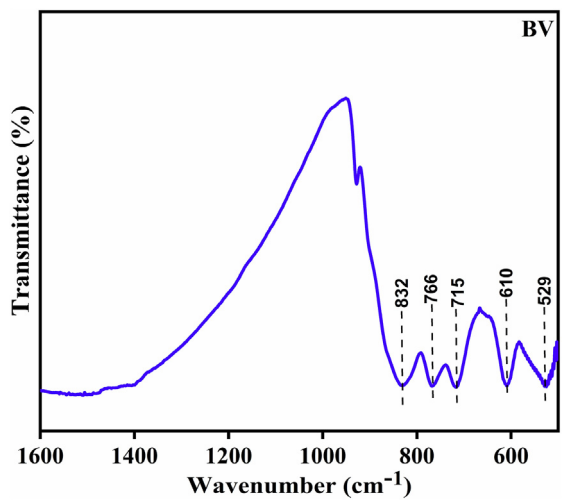

Fig. 3 – FTIR spectrum of BV sample.

The peaks at 832 depict asymmetric stretching vibration of the (V–O) bond while the peaks at 766, and 715 depict symmetric stretching vibration of the (V–O) bond [46,47]. The peaks are seen at 613, and 529 depicts the deformation of the vanadate anion (O–V–O) [48,49].

The surface morphology of the synthesized BV sample has been shown in Fig. 4 through SEM micrographs. Fig. 4(a–b) clearly show the presence of irregular-shaped grains of the BV. EDS elemental color mapping for the $Bi_2VO_{5.5}$ sample has been done for phase identification and Fig. 4(c) shows the selected area for the mapping. Fig. 4(d–f) shows the EDS elemental color mapping which affirms that Bi, V, and O elements are present.

To affirm the presence of the chemical state of the elements, an XPS analysis of the BV powdered sample was done. Fig. 5(a–c) present the XPS spectra which accords to the V2p, Bi4f, and O1s scans. Initially, deconvolution of the Bi4f spectrum was done into $Bi4f_{5/2}$ and $Bi4f_{7/2}$ asymmetric components, each deconvoluted into Bi^{3+} and Bi^{2+} components. The existing peaks observed at 158.7 and 164 eV correspond to the Bi^{3+} oxidation state and the presence of the peaks at 157.3 and 163.7 eV correspond to the Bi^{2+} oxidation state [50,51]. Firstly, deconvolution of the V2p spectrum was done into $V2p_{3/2}$ and $V2p_{1/2}$components, and each was further deconvoluted into V^{4+} and V^{5+} components. The presence of the peaks at 516.4 and 524.2 eV accords to the V^{5+} oxidation state and the presence of the peaks at 517.3 and 523 eV accords to the V^{4+}oxidation state [52]. Further, the asymmetric O1s spectrum was deconvoluted into O_L and O_A components [50]. Here, the presence of oxygen vacancies and lattice oxygen (O^{2-} oxidation state) have been symbolized by O_A and O_L. Localized oxygen vacancies are formed because of the intrinsic defects caused by thermal treatment during the material synthesis. Excess charge usually gets trapped in the form of electron pairs around the V and Bi atoms and at the vacancy site which causes a reduction of Bi^{3+} and V^{5+} to Bi^{2+} and V^{4+} respectively. Thus, we observe the simultaneous presence of Bi^{2+} and V^{4+} along with the existing Bi^{3+} and V^{5+} [53].

Time-dependent photocurrent response analysis of the $Bi_2VO_{5.5}$ was done to understand the phenomenon of charge carrier transportation as shown in Fig. 6. BV attains a low dark current density (~7.5 $\mu A/cm^2$) before dye degradation and on visible light illumination, the photocurrent density increases to ~12 $\mu A/cm^2$. Thus we evidence a light to dark current ratio of nearly 1.6 times. This high photocurrent density is because of the effective photogenerated charge carriers separation. The photocurrent is replicated for each irradiation as the photocurrent density response of the material is reversible [54,55].

Fig. 7(a) shows the DRS spectrum of the synthesized BV powder sample. The optical absorption edge of the BV can be seen in Fig. 7(a). The explored bandgap of the synthesized BV powdered sample is 2.13 eV as shown in Fig. 7(b). As the explored bandgap of the BV sample lies within the visible range, this allows photocatalysis assessment to be conducted in visible light irradiation.

Photocatalytic assessment of the BV powdered sample was measured by MB dye degradation as a pollutant and the results obtained are demonstrated in Fig. 8(a). Before commencing the photocatalysis assessment, adsorption saturation concerning the dye was attained precisely. MB dye degradation under visible light illumination was supervised by recording the decrement in the UV–visible absorption peak spectra of MB dye with an increase in illumination time which can be evidenced by Fig. 8(a). The decreased peak intensity with time supports that the pollutant solution has been decolorized. The $\frac{C}{C_o}$ vs time plots acquired with and without using BV powdered sample while photocatalysis assessment in visible light is shown in Fig. 8(b). Photolysis phenomena caused control dye without the usage of any sample, to attain ~ 27% MB dye degradation in 240 min of visible light illumination. BV sample attained ~ 70% degradation efficiency in 240 min during photocatalysis experiment. An improvement of 43% in degradation efficiency during photocatalysis was evidenced with the use of a BV powdered sample concerning the control dye without sample usage. Fig. 8(c) demonstrate the MB dye degradation percentage as ~ 70%, 68%, 65% and 63% with each advancing cycle. We observe no severe loss in photocatalytic efficiency even after 4 cycles which proclaims reusability of the BV powdered sample.

The piezocatalytic efficiency of the BV powdered sample was measured by MB dye degradation as a pollutant and the results obtained are demonstrated in Fig. 9(a). Before commencing the piezotocatalysis assessment, adsorption saturation concerning the dye was attained precisely. MB dye degradation under ultrasonication was supervised by recording the decrement in the absorption peak spectra of the MB dye with a surge in ultrasonication time which can be evidenced by Fig. 9(a). The decreased peak spectra with time support that the pollutant solution has been decolorized. The $\frac{C}{C_o}$ vs time plots obtained with BV sample and without utilizing sample while piezocatalysis assessment is shown in Fig. 9(b). The ultrasonication process causes water bubble formation (where water vapor and entrapped gases reside), its growth, and collapsing [56]. This activity creates a local hot spot where there is evidenced an increase in temperature up to 4000–5000K [56,57]. As a consequence of these localized hot spots, •OH radicals are created because of the thermolytic decomposition of water. These erupted •OH radicals further cause MB dye to degrade. This whole phenomenon is mentioned in literature as sonolysis

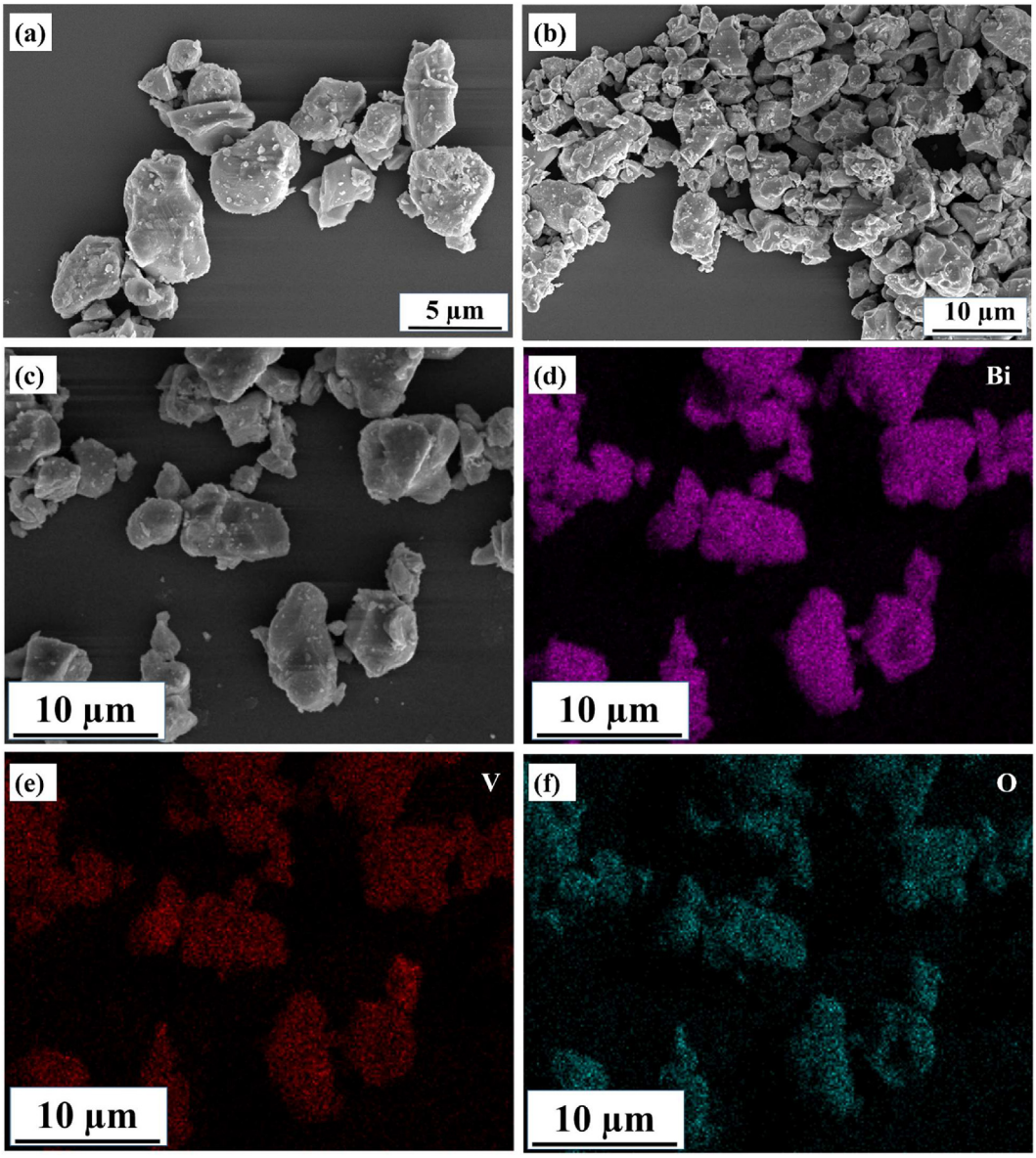

Fig. 4 – (a–b) SEM images of BV powdered sample, (c–f) EDS elemental color mapping analysis of BV.

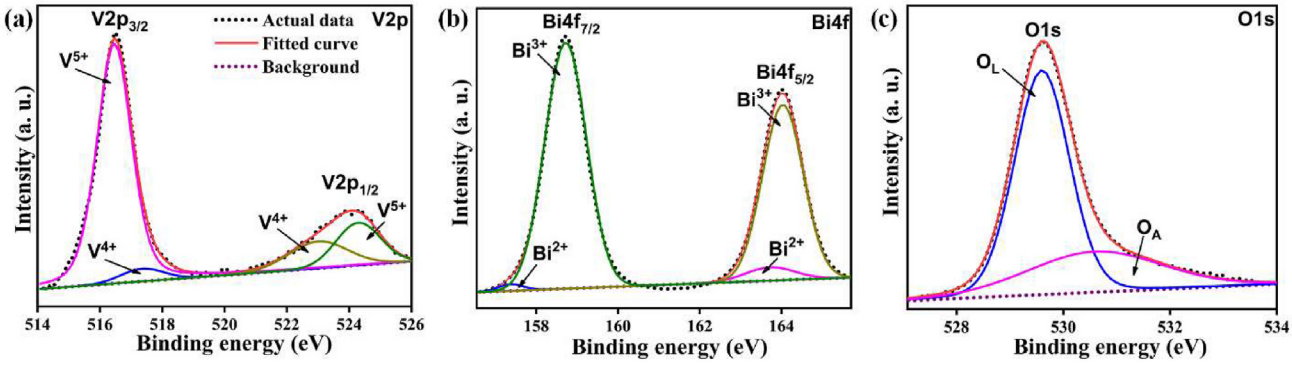

Fig. 5 – XPS spectra obtained for (a) V2p, (b) Bi4f, and (c) O1s.

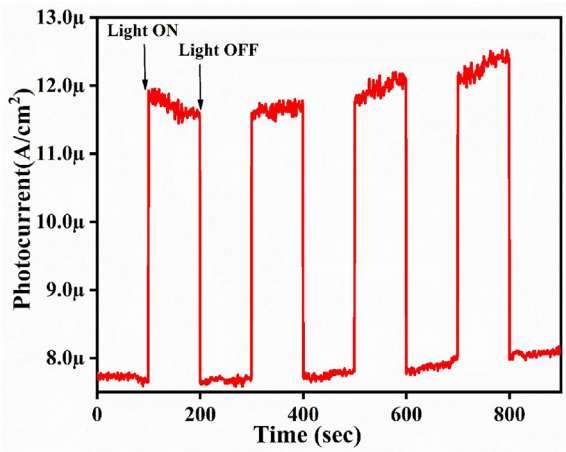

Fig. 6 – Current response vs. time for BV.

[58,59]. Since the water was used as a medium during ultrasonication so, after elapse of every 15 min, the water was replaced from the ultrasonicator in order to shun dye solution heating. The control dye without the usage of any sample incurs ~ 17% MB dye degradation in 240 min of ultrasonication. BV powdered sample achieved ~ 58% degradation efficiency within 240 min during the piezocatalysis experiment. An improvement of 41% in degradation efficiency during piezocatalysis was evidenced by using BV powdered sample concerning the control dye without sample.

The piezo-photocatalytic efficiency of the BV powdered sample was measured by MB dye degradation as a pollutant in the dual action of visible light and ultrasonication and the outcome obtained is exhibited in Fig. 10(a). Before commencing the piezo-photocatalysis assessment, adsorption saturation concerning the dye was attained precisely. MB dye degradation under piezo-photocatalysis was supervised by recording the decrement in the absorption peak spectra of MB dye with an increase in time which can be evidenced by Fig. 10(a). The decreased peak intensity with time supports that the pollutant solution has been decolorized. The ultrasonication process causes water bubble formation (where water vapor and entrapped gases reside), its growth, and collapsing. This activity creates a local hot spot where there is evidenced an increase in temperature up to 4000–5000K [56,57]. As a consequence of these localized hot spots, •OH radicals are created because of the thermolytic decomposition of water. These erupted •OH radicals further cause MB dye to degrade [58]. Since the water was used as a medium during the piezo-photocatalysis experiment so, after elapse of every 15 min, the water was replaced from the ultrasonicator in order to shun dye solution heating. The $\frac{C}{C_o}$ vs time plots obtained with and without using BV powdered sample during the piezo-photocatalysis assessment are shown in Fig. 10(b). The control dye without the usage of any sample incurs ~ 34% MB dye degradation in 240 min during the piezo-photocatalysis experiment. BV sample attained ~ 82% degradation efficiency within 240 min during the piezo-photocatalysis experiment. An improvement of 48% in degradation efficiency during piezo-photocatalysis was evidenced with the use of a BV powdered sample concerning the control dye without sample usage. The $\frac{C}{C_o}$ vs time plots obtained using BV powdered sample while photocatalysis, piezocatalysis, and piezo-photocatalysis assessment are displayed in Fig. 10(c). The dye degradation efficiency of ~ 70%, ~ 58%, and ~ 82% is attained with the use of BV powdered sample during photocatalysis, piezocatalysis, and piezo-photocatalysis assessment respectively. Clearly, it can be evidenced that better degradation efficiency was attained by the combined effect of piezo-photocatalysis than that was possible to achieve through individual piezocatalysis and individual photocatalysis experiments. Here, the dye degradation efficiency attained during piezocatalysis was less as compared to photocatalysis because of fewer charge carriers evolution in the absence of visible light illumination. An improvement of 20% and 41% in degradation performance during photocatalysis and piezo-photocatalysis respectively was evidenced with the use of a BV powdered sample concerning that attained by the individual piezocatalysis experiment. During piezo-photocatalysis assessment, better utilization of generated charge carriers takes place due to the modified band structure caused by the built-in electric field [60,61]. Moreover, existing polarization also depletes the possibility of charge recombination by efficient separation of charge carriers [60,62,63]. Thus, the dual effect of piezo-photocatalysis

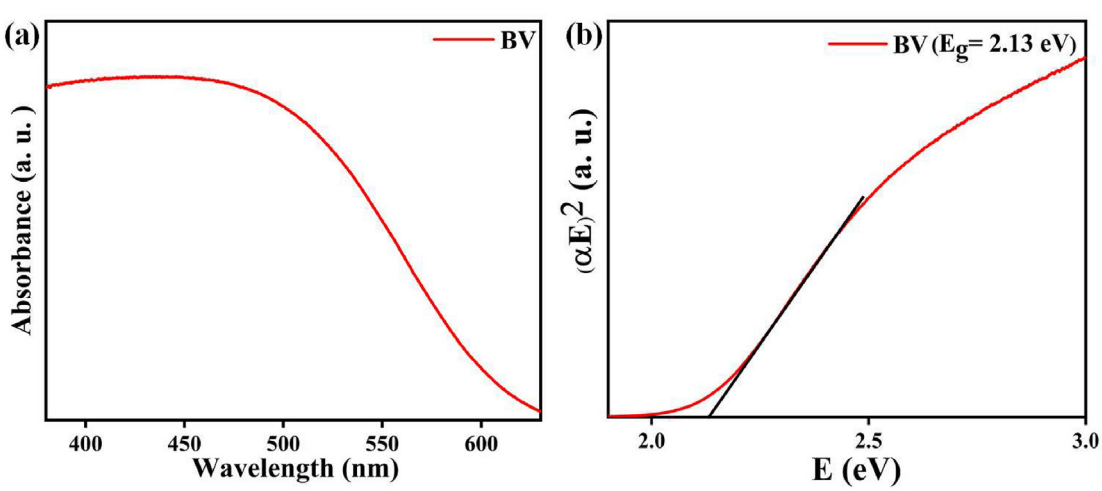

Fig. 7 – (a) Absorbance spectrum of the BV powdered sample, and (b) The Bandgap assessment using Tauc's plots.

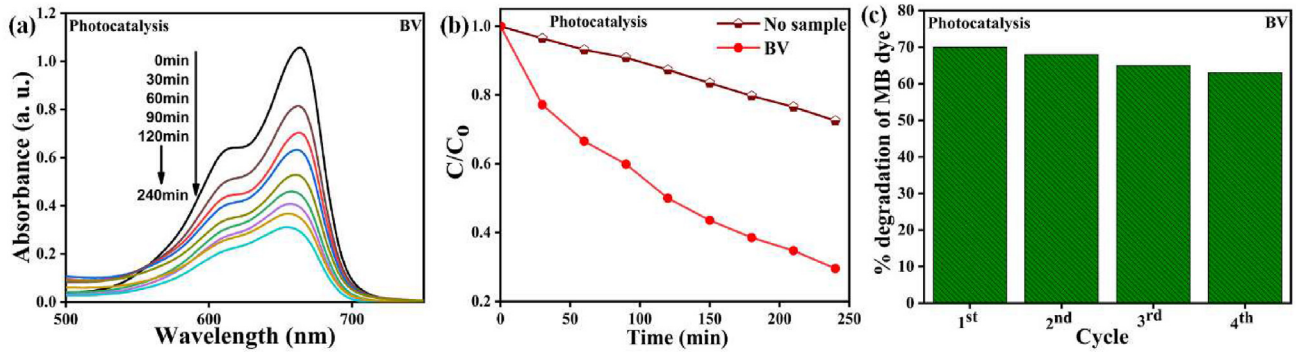

Fig. 8 – (a) Absorption spectra change while photocatalytic assessment utilizing BV powdered sample, (b) $\frac{C}{C_o}$ vs time plots for the photocatalytic assessment with sample and without utilizing any sample, (c) Repeated photocatalysis assessment of BV sample over four cycles.

could prove to be an efficient way to obtain enhanced photocatalytic efficiency. During the piezo-photocatalysis experiment, in view to capture active radical species such as hydroxyl radical (•OH), superoxide radical (• O_2^-), and holes (h^+), scavengers such as isopropanol (IPA), p-benzoquinone (p-BQ), and ethylenediaminetetraacetic acid (EDTA) respectively were introduced separately to the dye solution [64–66]. Fig. 10(d) demonstrates that the EDTA scavenger that scavenges holes (h^+) has put a major impact on the piezo-photocatalysis assessment. As per the scavenger test, holes (h^+) are considered the principal active species in the piezo-photocatalytic dye degradation activity.

Table 1 demonstrates piezo-photocatalytic dye degradation assessment using different catalysts. The $\frac{C}{C_o}$ vs time plots obtained using BV powdered sample in varied dye concentrations (5, 10, and 15 mg/L) during the piezo-photocatalysis assessment are shown in Fig. 11(a). The -ln $\left(\frac{C}{C_o}\right)$ vs time plots obtained using BV powdered sample in varied dye concentrations during the piezo-photocatalysis assessment are shown in Fig. 11(b). Here, the piezo-photocatalytic degradation reaction follows the pseudo-first-order kinetic according to Eq. (3) [67,68].

$$\ln\frac{C}{C_o} = -kt \tag{3}$$

Here, 'k' symbolizes the kinetic rate constant calculated by the slope of the $-\ln\frac{C}{C_o}$ vs time 't' linear plot. Here, 5 mg/L dye concentration attains the highest k value of 0.00528 min^{-1} and undergoes a reduction in k value with an increase in dye concentration. With varied dye concentration of 5, 10, 15 mg/L, the kinetic rate constant obtained was 0.00528, 0.0030, and 0.00125 min^{-1}, respectively. The graph between kinetic rate constant 'k' distinct MB dye concentration (5, 10, 15 mg/L) has been displayed in Fig. 11(c).

A simple germination index (GI) test was performed where the germination of seeds and their overall growth were analyzed in order to explore the reusability, sustainability, and suitability of the cleaned waste water post the piezo-photocatalysis experiment. 10 seeds of the Vigna radiata were placed in each of the 3 vials and were sprinkled with 0.5 ml of untreated, treated, and distilled water every day. The test analysis was done for a period of 7 days at IIT Mandi, India where the environmental temperature was 30 °C. Fig. 12(a–c) present seed growth with the use of dye water before piezo-photocatalysis, post piezo-photocatalysis, and with the use of distilled water.

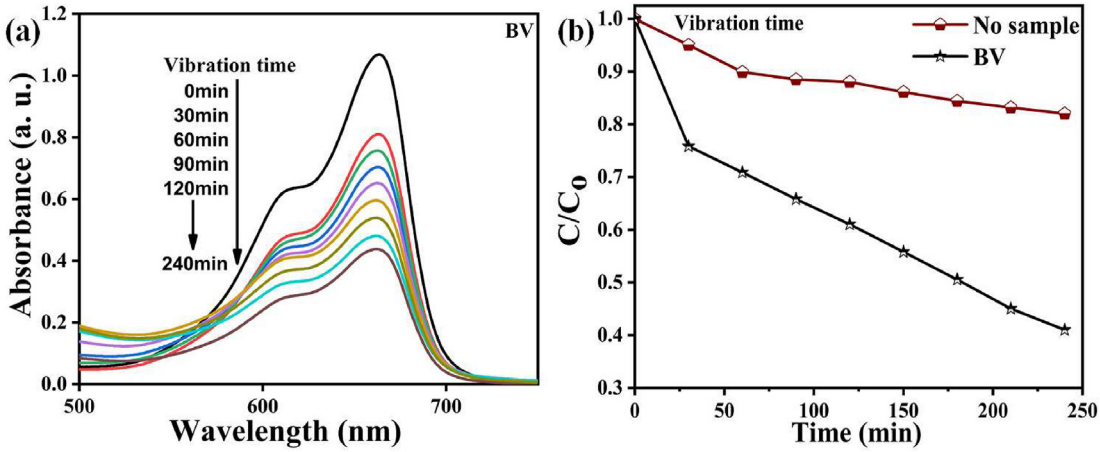

Fig. 9 – (a) Absorption spectra change while piezocatalytic assessment utilizing BV powdered sample, (b) $\frac{C}{C_o}$ vs time plots for the piezocatalytic dye degradation with sample and without utilizing any sample.

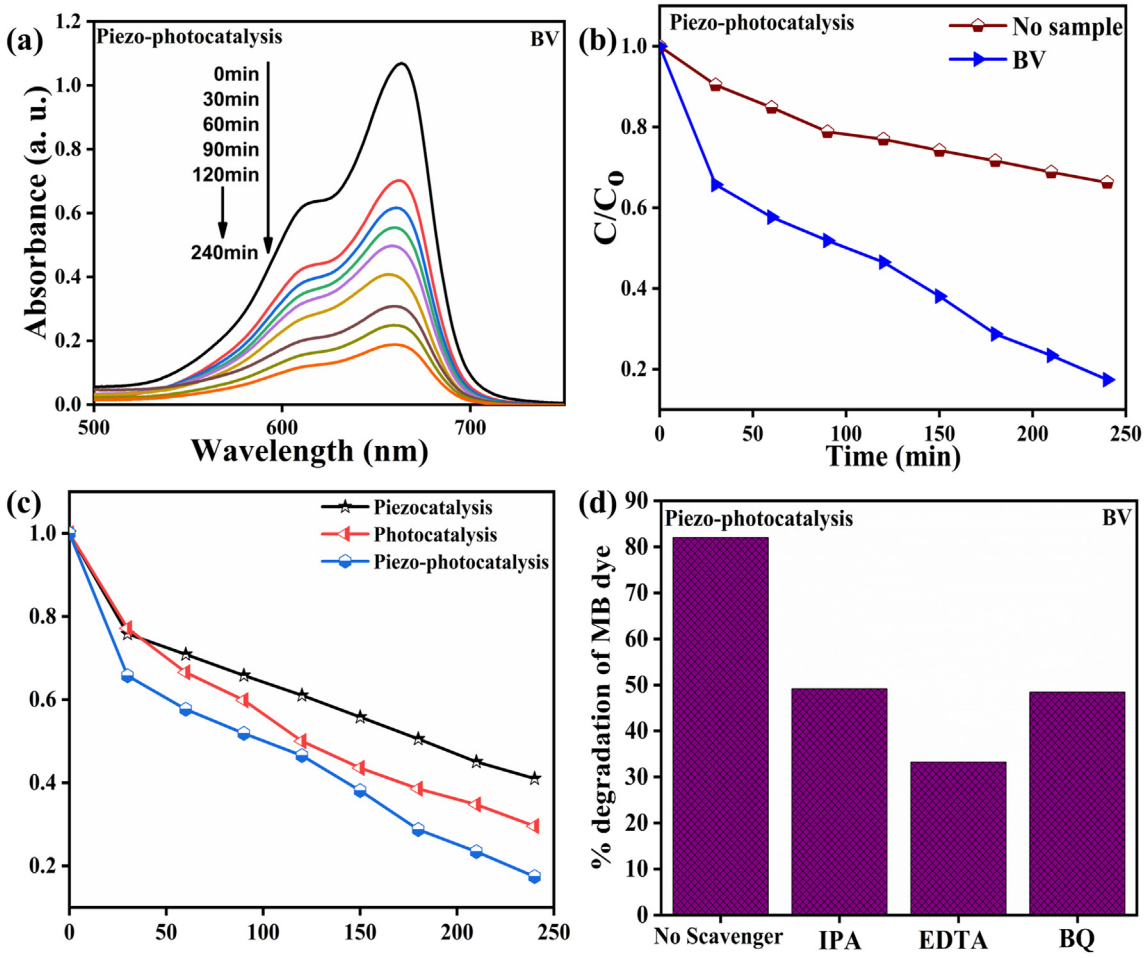

Fig. 10 – (a) Absorption spectra change while piezo-photocatalytic assessment utilizing BV powders, (b) $\frac{C}{C_o}$ vs time plots for the piezo-photocatalytic dye degradation with sample and without utilizing any sample, (c) $\frac{C}{C_o}$ vs time plots obtained using BV powdered sample during the photocatalysis, piezocatalysis, and piezo-photocatalysis assessment, (d) varied scavengers effect while piezo-photocatalytic assessment utilizing BV powders.

Table 1 – The piezo-photocatalytic dye degradation assessment using different catalysts.

Catalyst	Pollutant	Energy source (L- light)	Starting dye concentration (volume used)	Catalysis Time (min)	% Degradation
BiOCl [69]	Rhodamine B (RB dye)	Ultrasonic:120 W, 40 kHz; L: Xe Lamp	50 mg/L (50 mL)	96	~99%
Ag–$BaTiO_3$ [70]	RB dye	Ultrasound; L: Xe Lamp	0.01 mM (50 mL)	75	~83%
$Bi_2VO_{5.5}$ (Present study)	MB	Ultrasonic:120 W, 40 kHz; L: Xe Lamp	5 mg/L (10 mL)	240	~82%
ZnO/TiO_2 [71]	Methyl orange (MO dye)	Ultrasound:40 kHz L: Mercury Lamp	10 mg/L (50 mL)	120	~98%
PMN-PT@TiO_2 [72]	RB dye	Ultrasound:53 kHz, 180 W L: 15W ($\lambda < 254$ nm)	12 mg/L (50 mL)	210	~100%
Ag_2O/$BaTiO_3$ [73]	MO	Ultrasound:45 kHz, 500 W L: Xe Lamp	10 mg/L	120	~97%
$Bi_{0.5}Na_{0.5}TiO_3$@TiO_2 [74]	RB dye	Ultrasonic:100 W, 40 kHz; L: visible light	10 mg/L (50 mL)	90	~97%
BiOI/ZnO [75]	Bisphenol A	Ultrasonic:90 W, 40 kHz; L: Xe Lamp	10 mg/L (50 mL)	30	~100%
$BiVO_4$ [37]	MB dye	Ultrasonic:70 W, 40 kHz; L: Visible Light	5 mg/L (10 mL)	240	~81%
$BaZr_{0.02}Ti_{0.98}O_3$ [76]	RB dye	Ultrasonic:70 W, 40 kHz; L: UV Light	6 mg/L (10 mL)	240	~89%
ZnO nanoparticles [77]	RB dye	Ultrasonic:120 W, 40 kHz; L: UV Light	5 mg/L (100 mL)	120	~90%

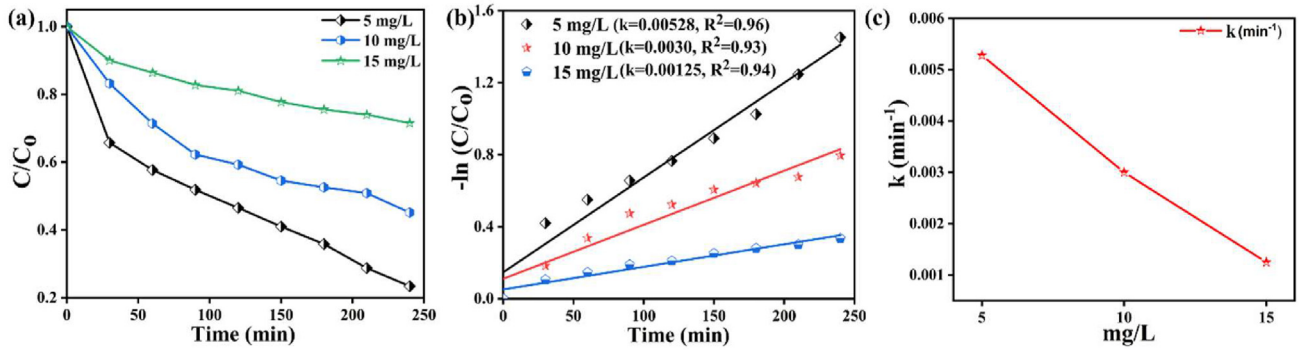

Fig. 11 – (a) $\frac{C}{C_o}$ vs time plots obtained using BV powdered sample in varied dye concentrations for piezo-photocatalytic, (b) plots between -ln $\left(\frac{C}{C_o}\right)$ vs time in varied dye concentration for piezo-photocatalytic assessment and, (c) plot between the kinetic rate constant 'k' vs MB dye concentration (mg/L).

It was noted that most hindrances to seed growth were seen with untreated 5 mg/L dye while growth with treated water falls under non-toxic level [78]. Although, edible plants need extra safety and their unfavorable effect needs to be tackled effectively. We suggest that this treated wastewater could be useful for watering playgrounds instead of edible plants [79]. In this way, there will be a partial reduction in water requirement. Phytotoxicity results have been shown in Fig. 12(d). To analyze compounds based on GI values Emino et. *al* and Zucconi et *al* have suggested three classifications as the absence of phytotoxicity (GI > 80%), moderate phytotoxicity (50% < *GI* < 80%), and high phytotoxicity (GI < 50%) [80,81]. As per the results, treated water lies at a moderate level of toxicity while untreated dye lies at a high toxicity level [81,82]. Here, the treated water used for seed germination has only attained 63% dye degradation efficiency after piezo-photocatalysis assessment. There is a further possibility to improve the germination index by achieving 100% purification efficiency of dye through enhancing catalytic load, catalytic time duration, and reduction in dye concentration [83,84].

Fig. 13(a–c) show a descriptive mechanism for MB dye degradation during photocatalysis, piezocatalysis, and piezo-photocatalysis experiments. Fig. 13(a) presents the mechanism of photocatalysis, where visible light induces the generation of electron (e^-)-hole (h^+) pairs in the BV phase. Hydroxyl radicals ($OH^\bullet$) are generated due to the oxidation of the adsorbed water by the holes while superoxide radicals ($O_2^{\bullet-}$) are generated since electrons react with adsorbed oxygen. The species like ($O_2^{\bullet-}$) and ($OH^\bullet$) are termed as reactive oxidizing species (ROS) which cause degradation of MB dye into harmless end products. Thus, photocatalytic activity takes place [18,37,85].

Fig. 13(b) presents the mechanism of piezocatalysis. The cavitation phenomenon causes local hot spot formation which in turn acts on the BV surface producing local strain [58]. Polarization charges (internal electric field) are induced on the BV surface as a result of the stress induced during ultrasonication. The free hole and electron pairs move to the opposite polarity under the influence of the internal electric field and thus assist in the separation of e^-–h^+ pairs [86,87]. This suppresses the possibility of recombination of charge carriers and thereby causes more free

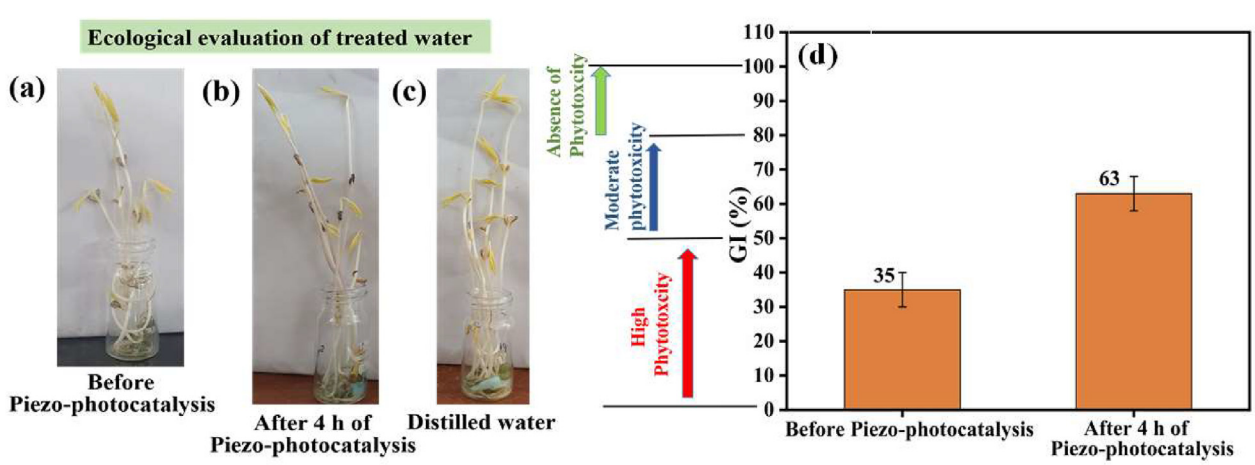

Fig. 12 – Impact of MB dye on Vigna radiata seeds growth evaluated for 7 days; Analysis is commenced utilizing (a) 5 mg/L MB dye, (b) treated wastewater, (c) distilled water, (d) Germination index investigated on 2 samples post 0 and 4 h of piezo-photocatalysis.

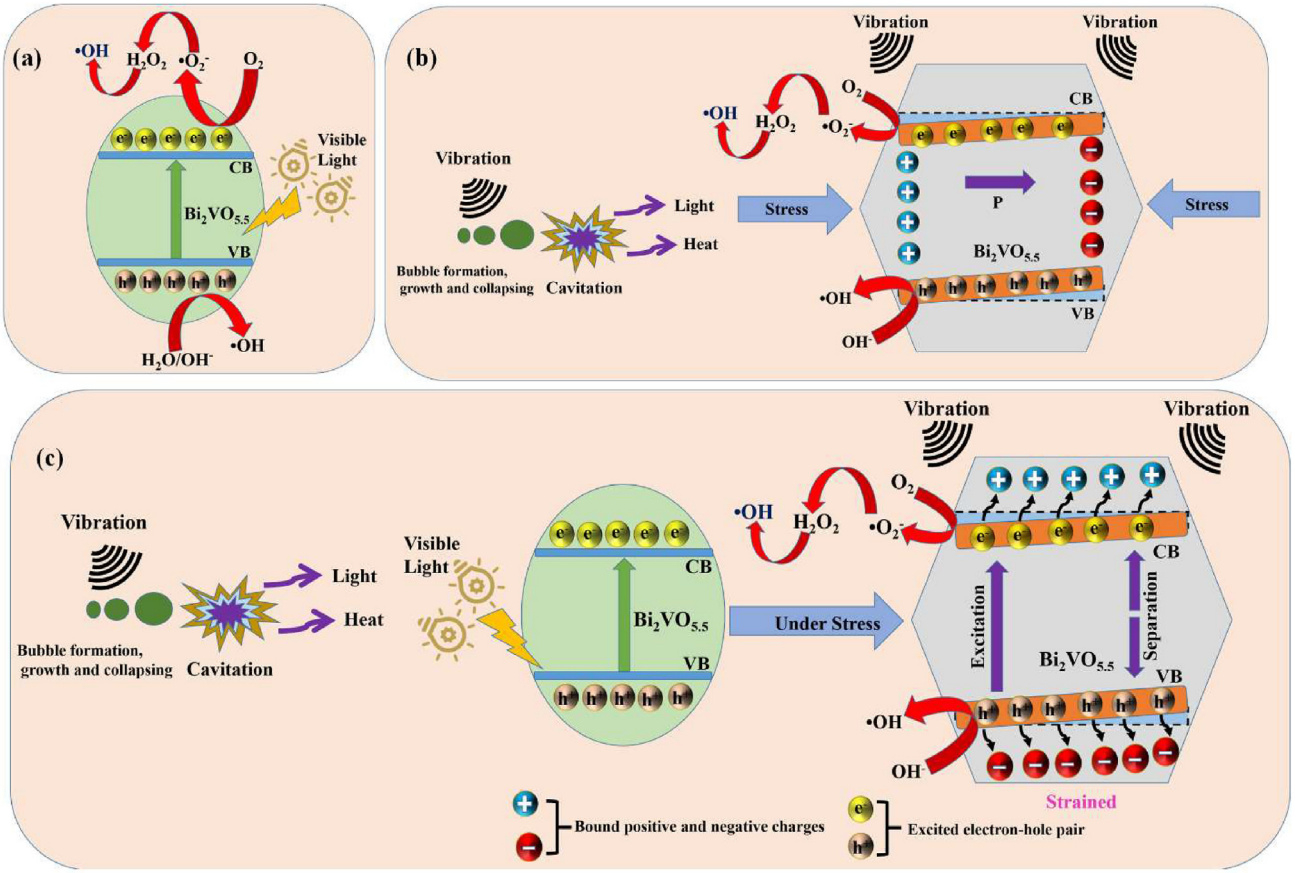

Fig. 13 – Schematic of the BV powdered sample for (a) photocatalysis, (b) piezocatalysis, (c) piezo-photocatalysis assessment.

charge accumulation on the BV surface [63,88]. Origination of the charge carriers while the ultrasonication process is still a matter of discussion, although it is believed that sonoluminescence (at 375 nm wavelength, light is generated during ultrasonication) and thermal rise because of hot spot formation may be the cause [89,90]. There may be a combined effect of phenomena like polarization or ultrasonication. Further, polarization also causes band bending which helps in the transfer of e^- and h^+ to the BV surface [74]. As the piezocatalysis is done in a dark environment, these aren't photogenerated e^- and h^+. Hydroxyl radicals ($OH^\bullet$) are generated due to the oxidation of the adsorbed water by the holes while superoxide radicals ($O_2^{\bullet-}$) are generated since electrons react with adsorbed oxygen. These ROS further cause the degradation of MB dye into harmless end products [37,56,57]. Thus, piezocatalytic activity takes place.

Fig. 13(c) presents the mechanism of the piezo-photocatalysis process. Visible light excites valence band (VB) electrons to the conduction band (CB) while leaving holes back in the VB and thus erupts electron (e^-)-hole (h^+) pairs in the BV phase [91]. Origination of the charge carriers while the ultrasonication process is still a matter of discussion, although it is believed that sonoluminescence and thermal rise because of hot spot formation may be the cause [89,90]. There could be a combined effect of phenomena like polarization or ultrasonication. During piezo-photocatalysis, photoexcited electrons and holes are in minor concentration while thermally exciting holes and electrons are in majority. Thus, the introduction of visible light along with ultrasonication enhances free charge concentration over the surface of the semiconductor catalysts [92]. Polarization charges are induced on the BV surface because of the stress induced during ultrasonication. The cavitation phenomenon causes local hot spot formation which in turn acts on the BV surface producing local strain [56,57]. Further, polarization also causes band bending which further causes photoexcited electrons to move to the lower energy level and the photogenerated holes in the VB move to the higher energy level [74]. The prevailing polarization cause holes and electrons to migrate in the opposite direction thus suppressing their recombination by enhancing the space between the charge carriers [87]. This ensures more availability of electrons and holes over the BV surface causing more radical formation [63]. Thus, the catalytic redox reaction is enhanced and thereby accelerating the dye degradation efficiency. Hydroxyl radicals ($OH^\bullet$) are generated due to the oxidation of the adsorbed water by the holes while superoxide radicals ($O_2^{\bullet-}$) are generated since electrons react with adsorbed oxygen. These ROS further cause the degradation of MB dye into harmless end products [37,56,57,90]. Thus, piezo-photocatalytic activity takes place.

4. Conclusions

The $Bi_2VO_{5.5}$ powder was proclaimed through solid-state synthesis at 750 °C in 8 h and their combined piezocatalytic and photocatalytic activity was explored to obtain enhanced piezo-photocatalytic efficiency. The catalyst adequately used both the visible light illumination and the ultrasonication for dye degradation by effectively separating charge carriers. A comparative study on the dye degradation efficiency attained through photocatalysis, piezocatalysis, and piezo-photocatalysis was done along with their degradation mechanism. The dye degradation efficiency of ~ 82% is attained with the use of a BV powdered sample during the piezo-photocatalysis experiment. Here, the dye degradation obeys pseudo first-order kinetic and attains the highest k value of 0.00528 min^{-1}. Thus, piezo-photocatalysis using $Bi_2VO_{5.5}$ could be an alternate way to attain higher MB dye degradation efficiency by combining the effect of both photocatalysis and piezocatalysis.

Data availability

All relevant data are available in this manuscript.

Declaration of Competing Interest

The authors declare that they have no known competing financial interests or personal relationships that could have appeared to influence the work reported in this paper.

Acknowledgments

The authors express their gratitude to Princess Nourah bint Abdulrahman University Researchers Supporting Project (Grant No. PNURSP2022R124), Princess Nourah bint Abdulrahman University, Riyadh, Saudi Arabia. The authors extend their appreciation to the Deanship of Scientific Research at King Khalid University, Saudi Arabia for funding this work through Large Research Groups Program under grant number L.R.G.P2/173/43.

This work was supported by the Korea Institute of Energy Technology Evaluation and Planning (KETEP) and the Ministry of Trade, Industry & Energy (MOTIE) of the Republic of Korea (No. 2018201010636A and 20204010600090).

REFERENCES

[1] Singh S, Sharma A, Malviya R. Industrial wastewater: Health concern and treatment strategies. Open Biol J 2021;9.

[2] Briffa J, Sinagra E, Blundell R. Heavy metal pollution in the environment and their toxicological effects on humans. Heliyon 2020;6:e04691.

[3] Titchou FE, Zazou H, Afanga H, El Gaayda J, Akbour RA, Nidheesh PV, et al. Removal of organic pollutants from wastewater by advanced oxidation processes and its combination with membrane processes. Chem Eng Process Intensif 2021;169:108631.

[4] Mizutani M, Palermo EF, Thoma LM, Satoh K, Kamigaito M, Kuroda K. Design and synthesis of self-degradable antibacterial polymers by simultaneous chain-and step-growth radical copolymerization. Biomacromolecules 2012;13:1554–63.

[5] Zhiyong Y, Mielczarski E, Mielczarski J, Laub D, Buffat P, Klehm U, et al. Preparation, stabilization and characterization of TiO_2 on thin polyethylene films (LDPE). Photocatalytic applications. Water Res 2007;41:862–74.

[6] Naseem T, Durrani T. The role of some important metal oxide nanoparticles for wastewater and antibacterial applications: a review. Environ Chem Ecotoxicol 2021;3:59–75.

[7] Park H, Hira SA, Muthuchamy N, Park S, Park KH. Synthesis of silver nanostructures in ionic liquid media and their application to photodegradation of methyl orange. Nanomater Nanotechnol 2019;9:1847980419836500.

[8] Di Paola A, García-López E, Marcì G, Palmisano L. A survey of photocatalytic materials for environmental remediation. J Hazard Mater 2012;211:3–29.

[9] Tang J, Zou Z, Ye J. Efficient photocatalytic decomposition of organic contaminants over $CaBi_2O_4$ under visible-light irradiation. Angew Chem 2004;116:4563–6.

[10] Poolwong J, Kiatboonyarit T, Achiwawanich S, Butburee T, Khemthong P, Kityakarn S. Three-dimensional hierarchical porous TiO_2 for enhanced adsorption and photocatalytic degradation of remazol dye. Nanomaterials 2021;11:1715.

[11] Huang B, Yang W, Wen Y, Shan B, Chen R. Co_3O_4-modified TiO_2 nanotube arrays via atomic layer deposition for improved visible-light photoelectrochemical performance. ACS Appl Mater Interfaces 2015;7:422–31. 0.

[12] Zhao L, Chen X, Wang X, Zhang Y, Wei W, Sun Y, et al. One-step solvothermal synthesis of a carbon@TiO_2 dyade structure effectively promoting visible-light photocatalysis. Adv Mater 2010;22:3317.

[13] Kallawar GA, Barai DP, Bhanvase BA. Bismuth titanate based photocatalysts for degradation of persistent organic compounds in wastewater: a comprehensive review on synthesis methods, performance as photocatalyst and challenges. J Clean Prod 2021;318:128563.

[14] Chen P, Liu H, Cui W, Lee SC, Wang L, Dong F. Bi-based photocatalysts for light-driven environmental and energy applications: structural tuning, reaction mechanisms, and challenges. EcoMat 2020;2:e12047.

[15] Song S, Xing Z, Zhao H, Li Z, Zhou W. Recent advances in bismuth-based photocatalysts: environment and energy applications. Green Energy Environ 2022. https://doi.org/10.1016/j.gee.2022.04.004.

[16] Kumar S, Sahare PD. Photocatalytic activity of bismuth vanadate for the degradation of organic compounds. Nano 2013;8:1350007.

[17] Wen X-J, Lv X-X, Sun J, Guo J, Fei Z-H, Niu C-G. Photocatalytic degradation of sulfamethazine using a direct Z-Scheme AgI/$Bi_4V_2O_{11}$ photocatalyst: mineralization activity, degradation pathways and promoted charge separation mechanism. J Hazard Mater 2020;385:121508.

[18] Zhao Y, Liu X, Gu S, Liu J. Enhanced photocatalytic performance of rhodamine B and enrofloxacin by Pt loaded $Bi_4V_2O_{11}$: boosted separation of charge carriers, additional superoxide radical production, and the photocatalytic mechanism. RSC Adv 2021;11:9746–55.

[19] Xie W, Zhong L, Wang Z, Liang F, Tang X, Zou C, et al. Photocatalytic performance of $Bi_2VO_{5.5}$/Bi_2O_3 laminated composite films under simulated sunlight irradiation. Solid State Sci 2019;94:1–7.

[20] Varma KBR, Subbanna GN, Guru TN, Rao CNR. Synthesis and characterization of layered bismuth vanadates. J Mater Res 1990;5:2718–22.

[21] Kumari N, Krupanidhi SB, Varma KBR. Structural, ferroelectric and optical properties of $Bi_2VO_{5.5}$ thin films deposited on platinized silicon {(100) Pt/TiO_2/SiO_2/Si} substrates. Appl Phys A 2008;91:693–9.

[22] Prasad KVR, Varma KBR, Raju AR, Satyalakshmi KM, Mallya RM, Hegde MS. Growth and ferroelectric properties of $Bi_2VO_{5.5}$ thin films with metallic $LaNiO_3$ electrodes. Appl Phys Lett 1993;63:1898–900.

[23] Ramasesha SK, Prasad KVR, Shankar M V, Varma KBR. The Dielectric Properties of Ferroelectric Bismuth Vanadate, BigVO; under Pressure n.d.

[24] Touboul M, Lokaj J, Tessier L, Kettman V, Vrabel V. Structure of dibismuth vanadate $Bi_2VO_{5.5}$. Acta Crystallogr Sect C Cryst Struct Commun 1992;48:1176–9.

[25] Tripathy D, Pandey A. Studies on structural and optical properties and its correlation with the ionic conductivity of the $Bi_2VO_{5.5}$–based oxide ionic conductors. Solid State Ionics 2019;341:115038.

[26] Zhu Q, Hailili R, Xin Y, Zhou Y, Huang Y, Pang X, et al. Efficient full spectrum responsive photocatalytic NO conversion at $Bi_2Ti_2O_7$: Co-effect of plasmonic Bi and oxygen vacancy. Appl Catal B Environ 2022:121888.

[27] Akopjan AV, Serov TV, Dolgikh VA, Ardaschnikova EI, Lightfoot P. A new anion conductive bismuth–vanadium oxyfluoride. J Mater Chem 2002;12:1490–4.

[28] Abraham F, Boivin JC, Mairesse G, Nowogrocki G. The BIMEVOX series: a new family of high performances oxide ion conductors. Solid State Ionics 1990;40:934–7.

[29] Kendall KR, Navas C, Thomas JK, zur Loye H-C. Recent developments in oxide ion conductors: Aurivillius phases. Chem Mater 1996;8:642–9.

[30] Wang JM, Cao F, Lv X, Li S, Cai JJ, Qin GW. Synthesis of $BiVO_4$/$Bi_2VO_{5.5}$ heterogeneous nanostructures with enhanced visible light photocatalytic activity. Mater Sci Forum 2016;847:211–7. Trans Tech Publ.

[31] Xie W, Qin N, Li B, Bao D. Enhanced visible-light catalytic activity of Au nanoparticles loaded c-axis oriented $Bi_2VO_{5.5}$ porous thin films. Ceram Int 2015;41:8433–43.

[32] Liang M, Yang Z, Mei Y, Zhou H, Yang S. Dye-sensitized-assisted, enhanced photocatalytic activity of TiO_2/$Bi_4V_2O_{11}$. Nano 2018;13:1850028.

[33] Lu Y, Pu Y, Wang J, Qin C, Chen C, Seo HJ. On structure and methylene blue degradation activity of an Aurivillius-type photocatalyst of $Bi_4V_2O_{11}$ nanoparticles. Appl Surf Sci 2015;347:719–26.

[34] Li Z, Zhang Q, Wang L, Yang J, Wu Y, He Y. Novel application of Ag/$PbBiO_2I$ nanocomposite in piezocatalytic degradation of rhodamine B via harvesting ultrasonic vibration energy. Ultrason Sonochem 2021;78:105729.

[35] Joseph M, Lee HY, Tabata H, Kawai T. Ferroelectric behavior of epitaxial $Bi_2VO_{5.5}$ thin films on Si (100) formed by pulsed-laser deposition. J Appl Phys 2000;88:1193–5.

[36] Kumari N, Parui J, Varma KBR, Krupanidhi SB. C–V studies on metal–ferroelectric bismuth vanadate ($Bi_2VO_{5.5}$)–semiconductor structure. Solid State Commun 2006;137:566–9.

[37] Kumar M, Vaish R, ben Ahmed S. Piezo-photocatalytic activity of mechanochemically synthesized $BiVO_4$ for dye cleaning. J Am Ceram Soc 2022;105(3):2309–22. https://doi.org/10.1111/jace.18233.

[38] Zhang D, Su C, Yao S, Li H, Pu X, Geng Y. Facile in situ chemical transformation synthesis, boosted charge separation, and increased photocatalytic activity of $BiPO_4$/BiOCl pn heterojunction photocatalysts under simulated sunlight irradiation. J Phys Chem Solid 2020;147:109630.

[39] Shao Z, Meng X, Lai H, Zhang D, Pu X, Su C, et al. Coralline-like Ni2P decorated novel tetrapod-bundle $Cd_{0.9}Zn_{0.1}$SZB/WZ homojunctions for highly efficient visible-light photocatalytic hydrogen evolution. Chin J Catal 2021;42:439–49.

[40] Nabi G, Malik N, Raza W. Degradation effect of temperature variation and dye loading g-C3N4 towards organic dyes. Inorg Chem Commun 2020;119:108050. https://doi.org/10.1016/j.inoche.2020.108050.

[41] Albeladi SSR, Malik MA, Al-thabaiti SA. Facile biofabrication of silver nanoparticles using Salvia officinalis leaf extract and its catalytic activity towards Congo red dye degradation. J Mater Res Technol 2020;9:10031–44.

[42] Aadil M, Zulfiqar S, Sabeeh H, Warsi MF, Shahid M, Alsafari IA, et al. Enhanced electrochemical energy storage properties of carbon coated Co_3O_4 nanoparticles-reduced graphene oxide ternary nano-hybrids. Ceram Int 2020;46:17836–45.

[43] Aadil M, Zulfiqar S, Agboola PO, Aboud MFA, Shakir I, Warsi MF. Fabrication of graphene supported binary nanohybrid with multiple approaches for electrochemical energy storage applications. Synth Met 2021;272:116645.

[44] Ashraf N, Aadil M, Zulfiqar S, Sabeeh H, Khan MA, Shakir I, et al. Wafer-like CoS architectures and their nanocomposites with polypyrrole for electrochemical energy storage applications. ChemistrySelect 2020;5:8129–36.

[45] Patwe SJ, Patra A, Dey R, Roy A, Kadam RM, Achary SN, et al. Probing the local structure and phase transitions of $Bi_4V_2O_{11}$-based fast ionic conductors by combined Raman and XRD studies. J Am Ceram Soc 2013;96:3448–56.

[46] Dimitrov V, Dimitriev Y, Montenero A. IR spectra and structure of V_2O_5 GeO_2 Bi_2O_3 glasses. J Non-Cryst Solids 1994;180:51–7.

[47] Abd El-Moneim A. DTA and IR absorption spectra of vanadium tellurite glasses. Mater Chem Phys 2002;73:318–22.

[48] Tripathy D, Saikia A, Tado GT, Pandey A. Dielectric study of Ti-doped $Bi_2VO_{5.5}$ solid electrolyte. Indian J Phys 2019;93:845–59.

[49] Tripathy D, Saikia A, Pandey A. Effect of simultaneous Ti and Nb doping on structure and ionic conductivity of $Bi_2V_{1-x}Ti_{x/2}Nb_{x/2}O_{5.5-\delta}$ ($0.1\leq x\leq 0.25$) ceramics. Ionics (Kiel) 2019;25:2221–30.

[50] Lv C, Chen G, Zhou X, Zhang C, Wang Z, Zhao B, et al. Oxygen-induced Bi5+-self-doped $Bi_4V_2O_{11}$ with ap–n homojunction toward promoting the photocatalytic performance. ACS Appl Mater Interfaces 2017;9:23748–55.

[51] Liu Z, Niu J, Feng P, Sui Y, Zhu Y. One-pot synthesis of $Bi_{24}O_{31}Br_{10}$/$Bi_4V_2O_{11}$ heterostructures and their photocatalytic properties. RSC Adv 2014;4:43399–405.

[52] Anwar K, Naqvi FK, Beg S. Synthesis of tetragonally stabilized lanthanum doped bismuth vanadium oxide nanoparticles and its enhanced visible light induced photocatalytic performance. Phase Transitions 2022;95:64–79.

[53] Daelman N, Hegner FS, Rellán-Piñeiro M, Capdevila-Cortada M, García-Muelas R, López N. Quasi-degenerate states and their dynamics in oxygen deficient reducible metal oxides. J Chem Phys 2020;152:50901.

[54] Fan C-M, Peng Y, Zhu Q, Lin L, Wang R-X, Xu A-W. Synproportionation reaction for the fabrication of Sn^{2+} self-doped SnO_{2-x} nanocrystals with tunable band structure and highly efficient visible light photocatalytic activity. J Phys Chem C 2013;117:24157–66.

[55] Xia J, Liu W, Teng Y, Wang QS, Zhao L, Ruan MM. Highly monodisperse $Cu_3Mo_2O_9$ micropompons with excellent

performance in photocatalysis, photocurrent response and lithium storage. RSC Adv 2015;5:12015–24.
[56] Kumar M, Singh G, Vaish R. Reduced graphene oxide/bismuth vanadate composite as an efficient piezocatalyst for degradation of organic dye. Mater Adv 2021;2(12):4093–101. https://doi.org/10.1039/d1ma00284h.
[57] Singh KP, Singh G, Vaish R. Utilizing the localized surface piezoelectricity of centrosymmetric $Sr_{1-x}Fe_xTiO_3$ ($x \leq 0.2$) ceramics for piezocatalytic dye degradation. J Eur Ceram Soc 2021;41:326–34.
[58] Tezcanli-Güyer G, Ince NH. Individual and combined effects of ultrasound, ozone and UV irradiation: a case study with textile dyes. Ultrasonics 2004;42:603–9.
[59] Ghows N, Entezari MH. Kinetic investigation on sono-degradation of Reactive Black 5 with core–shell nanocrystal. Ultrason Sonochem 2013;20:386–94.
[60] Morris MR, Pendlebury SR, Hong J, Dunn S, Durrant JR. Effect of internal electric fields on charge carrier dynamics in a ferroelectric material for solar energy conversion. Adv Mater 2016;28:7123–8.
[61] Yang W, Yu Y, Starr MB, Yin X, Li Z, Kvit A, et al. Ferroelectric polarization-enhanced photoelectrochemical water splitting in TiO_2–$BaTiO_3$ core–shell nanowire photoanodes. Nano Lett 2015;15:7574–80.
[62] Dunn S, Tiwari D. Influence of ferroelectricity on the photoelectric effect of $LiNbO_3$. Appl Phys Lett 2008;93:92905.
[63] Yang Q, Wang W, Xu S, Wang ZL. Enhancing light emission of ZnO microwire-based diodes by piezo-phototronic effect. Nano Lett 2011;11:4012–7.
[64] Chuaicham C, Sekar K, Xiong Y, Balakumar V, Mittraphab Y, Shimizu K, et al. Single-step synthesis of oxygen-doped hollow porous graphitic carbon nitride for photocatalytic ciprofloxacin decomposition. Chem Eng J 2021;425:130502.
[65] Yu F, Gong F, Yang Q, Wang Y. Fabrication of a magnetic retrievable dual Z-scheme g-C3N4/$BiVO_4$/$CoFe_2O_4$ composite photocatalyst with significantly enhanced activity for the degradation of rhodamine B and hydrogen evolution under visible light. Diam Relat Mater 2022;125:109004.
[66] Prabakaran E, Velempini T, Molefe M, Pillay K. Comparative study of KF, KCl and KBr doped with graphitic carbon nitride for superior photocatalytic degradation of methylene blue under visible light. J Mater Res Technol 2021;15:6340–55.
[67] Singh RP, Khagar PS, Mourya AK, Warkhade SK, Zodape SP, Pratap UR, et al. Synthesis of $Ag_2V_4O_{11}$ nanoflakes mediated photoactivation of peroxymonosulfate ion for enhanced dye degradation and intrinsic bactericidal activity. Mater Sci Semicond Process 2022;143:106526.
[68] Sharma SS, Palaty S, John AK. Band gap modified zinc oxide nanoparticles: an efficient visible light active catalyst for wastewater treatment. Int J Environ Sci Technol 2021;18:2619–32. https://doi.org/10.1007/s13762-020-02976-7.
[69] Ismail M, Wu Z, Zhang L, Ma J, Jia Y, Hu Y, et al. High-efficient synergy of piezocatalysis and photocatalysis in bismuth oxychloride nanomaterial for dye decomposition. Chemosphere 2019;228:212–8. https://doi.org/10.1016/j.chemosphere.2019.04.121.
[70] Xu S, Liu Z, Zhang M, Guo L. Piezotronics enhanced photocatalytic activities of Ag-$BaTiO_3$ plasmonic photocatalysts. J Alloys Compd 2019;801:483–8.
[71] You H, Wu Z, Jia Y, Xu X, Xia Y, Han Z, et al. High-efficiency and mechano-/photo-bi-catalysis of piezoelectric-ZnO@photoelectric-TiO_2 core-shell nanofibers for dye decomposition. Chemosphere 2017;183:528–35.
[72] Dai B, Lu C, Kou J, Xu Z, Wang F. Photocatalytic performance of PMN-PT@TiO_2 highly enhanced by alternative spatial electric field induced charge separation effect. J Alloys Compd 2017;696:988–95.
[73] Zhao W, Zhang Q, Wang H, Rong J, Lei E, Dai Y. Enhanced catalytic performance of Ag_2O/$BaTiO_3$ heterostructure microspheres by the piezo/pyro-phototronic synergistic effect. Nano Energy 2020;73:104783.
[74] Xu X, Lin X, Yang F, Huang S, Cheng X. Piezo-photocatalytic activity of $Bi_{0.5}Na_{0.5}TiO_3$@TiO_2 composite catalyst with heterojunction for degradation of organic dye molecule. J Phys Chem C 2020;124:24126–34.
[75] Zhang C, Fei W, Wang H, Li N, Chen D, Xu Q, et al. Pn Heterojunction of BiOI/ZnO nanorod arrays for piezo-photocatalytic degradation of bisphenol A in water. J Hazard Mater 2020;399:123109.
[76] Sharma M, Singh G, Vaish R. Dye degradation and bacterial disinfection using multicatalytic $BaZr_{0.02}Ti_{0.98}O_3$ ceramics. J Am Ceram Soc 2020;103:4774–84.
[77] Lei H, Zhang H, Zou Y, Dong X, Jia Y, Wang F. Synergetic photocatalysis/piezocatalysis of bismuth oxybromide for degradation of organic pollutants. J Alloys Compd 2019;809:151840. https://doi.org/10.1016/j.jallcom.2019.151840.
[78] Priac A, Badot P-M, Crini G. Treated wastewater phytotoxicity assessment using Lactuca sativa: focus on germination and root elongation test parameters. C R Biol 2017;340:188–94.
[79] Singh A, Bhati A, Khare P, Tripathi KM, Sonkar SK. Soluble graphene nanosheets for the sunlight-induced photodegradation of the mixture of dyes and its environmental assessment. Sci Rep 2019;9:1–12.
[80] Emino ER, Warman PR. Biological assay for compost quality. Compost Sci Util 2004;12:342–8.
[81] Zucconi F, Monaco A, Forte M, Bertoldi M de. Phytotoxins during the stabilization of organic matter. Compost Agric Other Wastes 1985. Edited by JKR Gasser.
[82] Zeghioud H, Khellaf N, Amrane A, Djelal H, Bouhelassa M, Assadi AA, et al. Combining photocatalytic process and biological treatment for Reactive Green 12 degradation: optimization, mineralization, and phytotoxicity with seed germination. Environ Sci Pollut Res 2021;28:12490–9.
[83] Tu S, Guo Y, Zhang Y, Hu C, Zhang T, Ma T, et al. Piezocatalysis and piezo-photocatalysis: catalysts classification and modification strategy, reaction mechanism, and practical application. Adv Funct Mater 2020;30:1–31. https://doi.org/10.1002/adfm.202005158.
[84] Kumar A, Pandey G. A review on the factors affecting the photocatalytic degradation of hazardous materials. Mater Sci Eng Int J 2017;1:1–10.
[85] Kong X, Liu X, Zheng Y, Chu PK, Zhang Y, Wu S. Graphitic carbon nitride-based materials for photocatalytic antibacterial application. Mater Sci Eng R Rep 2021;145:100610.
[86] Zhao Z, Wei L, Li S, Zhu L, Su Y, Liu Y, et al. Exclusive enhancement of catalytic activity in $Bi_{0.5}Na_{0.5}TiO_3$ nanostructures: new insights into the design of efficient piezocatalysts and piezo-photocatalysts. J Mater Chem A 2020;8:16238–45. https://doi.org/10.1039/c9ta14007g.
[87] Zhu Q, Zhang K, Li D, Li N, Xu J, Bahnemann DW, et al. Polarization-enhanced photocatalytic activity in non-centrosymmetric materials based photocatalysis: a review. Chem Eng J 2021;426:131681.
[88] Feng W, Lin L, Li H, Chi B, Pu J, Li J. Hydrogenated TiO_2/ZnO heterojunction nanorod arrays with enhanced performance for photoelectrochemical water splitting. Int J Hydrogen Energy 2017;42:3938–46.

[89] Zhu L, Meng Z-D, Park C-Y, Ghosh T, Oh W-C. Characterization and relative sonocatalytic efficiencies of a new MWCNT and CdS modified TiO_2 catalysts and their application in the sonocatalytic degradation of rhodamine B. Ultrason Sonochem 2013;20:478–84.

[90] Lei H, Zhang H, Zou Y, Dong X, Jia Y, Wang F. Synergetic photocatalysis/piezocatalysis of bismuth oxybromide for degradation of organic pollutants. J Alloys Compd 2019;809:151840.

[91] Ganeshbabu M, Kannan N, Venkatesh PS, Paulraj G, Jeganathan K, MubarakAli D. Synthesis and characterization of $BiVO_4$ nanoparticles for environmental applications. RSC Adv 2020;10:18315–22.

[92] Lin E, Wu J, Qin N, Yuan B, Kang Z, Bao D. Enhanced piezocatalytic, photocatalytic and piezo-/photocatalytic performance of diphasic $Ba_{1-x}Ca_xTiO_3$ nanowires near a solubility limit. Catal Sci Technol 2019;9:6863–74.